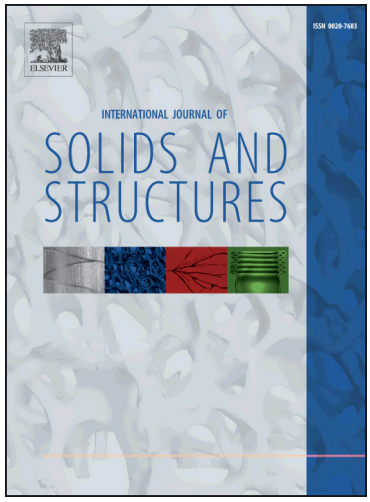

Multi-axial brittle failure criterion using Weibull stress for open Kelvin cell foams

D. Zhang, M. Abendroth, M. Kuna, J. Storm

PII: S0020-7683(15)00191-2
DOI: http://dx.doi.org/10.1016/j.ijsolstr.2015.04.020
Reference: SAS 8748

To appear in: *International Journal of Solids and Structures*

Received Date: 18 June 2014
Revised Date: 25 March 2015

Please cite this article as: Zhang, D., Abendroth, M., Kuna, M., Storm, J., Multi-axial brittle failure criterion using Weibull stress for open Kelvin cell foams, *International Journal of Solids and Structures* (2015), doi: http://dx.doi.org/10.1016/j.ijsolstr.2015.04.020

Multi-axial brittle failure criterion using Weibull stress for open Kelvin cell foams

D. Zhang [a, *], M. Abendroth [a], M. Kuna [a], J. Storm [a]

[a] TU Bergakademie Freiberg, Institute for Mechanics and Fluid Dynamics, Lampadiusstraße 4, 09596 Freiberg, Germany

Abstract

Foam structures have found an increasingly wide utilization in modern industry because of their porous geometric characteristic and favorable mechanical properties like lightness, high strength and so on. Elastic buckling, plastic yielding, brittle fracture and crushing are typical failure mechanisms of foam structures. The influences of foam geometry and morphology on the failure mechanisms are still not fully understand. In this paper the Kelvin cell model is used to simulate the foam structure and to study the influence of relative density and geometric properties on failure behavior. By extensive FEM analyses of representative volume elements under multi-axial loading with periodic boundary conditions the macroscopic failure limit surface is calculated in stress space. Locally at the microstructure the probabilistic Weibull model and the maximum principal stress criterion are used as failure criterion.

Key words: failure criterion, open-cell foam, Kelvin cell, Weibull stress criterion

1. Introduction

Foam structures are convenient light and stiff structures which preserve the high moduli and collapse strengths of the original materials but exhibit much lower densities. Foam structures are expected to have various engineering applications. For example, they are used in lightweight structural sandwich panels and in energy absorptions devices because of their low relative densities and high specific strengths (Ashby, 2000; Gibson and Ashby, 1999). In many applications they may be subjected to multi-axial loads. Foam structures can fail by several mechanisms like elastic buckling, plastic yielding, brittle crushing or brittle fracture depending on the properties of the original material which they are made of and on the relative density and the geometric properties (Jang et al., 2008; Jang and Kyriakides, 2009a, b). These mechanisms occur on the micro-structure

* Corresponding author. Tel.: +49 3731 393223; E-mail address: dongshuan.zhang@student.tu-freiberg.de

of foams, i.e. at struts and nodes (DeRuntz and Hoffman, 1969). The failure behavior on the macro-scale associated with all these mechanisms mentioned above has to be found by mechanical analyses. The mechanical behavior of foam structures, suitable homogenization methods and the influence of imperfection are discussed by several researchers (Deshpande and Fleck, 2000, 2001; Gibson et al., 1989; Sridhar and Fleck, 2005; Thiyagasundaram et al., 2010). The Kelvin cell is a simple geometry which is frequently used to simulate foam structure (Gong and Kyriakides, 2005; Gong et al., 2005a; Gong et al., 2005b; Jang et al., 2010; Mills, 2007; Sullivan and Ghosn, 2009; Sullivan et al., 2009; Takahashi et al., 2010).

With brittle foams, multi-axial loading situations are more complex to assess than for simple compact structures of homogeneous materials. The fracture of brittle materials initiates from flaws distributed in the material. The size of the flaws affects the strength, why in that case the strength of brittle materials should be expressed by a probability function. Weibull proposed a statistical theory of brittle fracture (Weibull, 1951). The experimental results also show that the fracture statistics of ceramics obeys Weibull distribution, that is why it is widely used in failure probability analysis (Amaral et al., 2007; Danzer et al., 2007; Karolczuk, 2013; Klein, 2009). For an inhomogeneous stress state, the Weibull stress introduced by Beremin (Beremin, 1983) plays an important role to characterize the failure strength and to predict the failure limit surface. It can be estimated from experiment (Fuis and Navrat, 2011; Gao et al., 1998; Lei Y, 1998; Minami et al., 1992; O'Dowd et al., 2000; Yin et al., 2004).

The failure of foam structures under multi-axial loading can be caused by different mechanism like stretching, bending and buckling. The yield criteria under different macroscopic loading are studied by many authors based on experimental observations and numerical simulation (Aghdam et al., 2000; Bigoni and Piccolroaz, 2004; C Chen, 1999; Demiray et al., 2007; Deshpande and Fleck, 2000, 2001; Piccolroaz and Bigoni, 2009; Takahashi et al., 2010). Altenbach (Altenbach et al., 2014) gives a summary on different yield and failure criteria and their limitations. But all the failure criteria mentioned above do not consider the failure probability, which is essentially for ceramic foams. In this paper, we are using the open cell Kelvin foam to simulate the foam structure made from a brittle material like ceramic and study the multi-axial failure behavior using a probabilistic Weibull model and for comparison the maximum principal stress as local failure criterion.

2. Model description

2.1 Kelvin cell foam models

The Kelvin cell, or tetrakaidecahedron, consists of six flat quadrilateral and eight hexagonal faces. The edges of all faces are considered as solid beams, which results in an open cell foam. The Kelvin cell in a body-centered cubic arrangement results in a partition of the 3D Euclidean space.

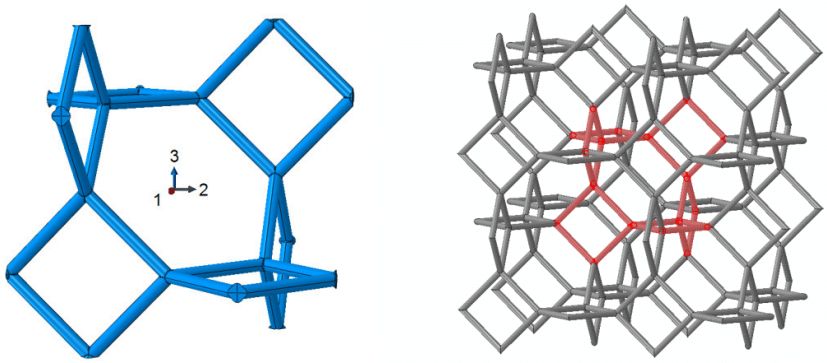

Fig. 1 A single representative volume element of a Kelvin cell and its periodic arrangement.

2.2 Homogenization

Due to the regularity of the Kelvin cell, some of the mechanical properties of interest for foam structure can be evaluated by considering just a single representative volume element (RVE) of a Kelvin cell foam (Dement'ev and Tarakanov, 1970; Gong and Kyriakides, 2005; Gong et al., 2005b; Jang et al., 2008; Laroussi et al., 2002; Mills, 2007; Warren and Kraynik, 1997; Zhu, 1997). Homogenization of a heterogeneous material is a process leading to its macroscopic characterization with fewer parameters than those needed for a full description of the object. On the meso-scale the structure is composed of periodic unit cells as representative volume elements (RVE). Within a homogenization volume V, which is bounded by surface A, the local displacements u_i can be written as

$$u_i = \bar{\varepsilon}_{ik} x_k + u_i^*, \tag{1}$$

where $\bar{\varepsilon}_{ik}$ are the homogenized global linear elastic strains, x_k the locations and u_i^* the displacement fluctuations. All homogenized or effective quantities are denoted by an upper bar. The displacement fluctuations exist due to the inhomogeneous local displacements inside the considered RVE. Differentiation of Eq. (1) and considering the symmetries of the strain tensor for small deformation problem we get for the average strain

$$\bar{\varepsilon}_{ik} = \frac{1}{V}\int_V \left\{\frac{1}{2}\left(u_{i,k} + u_{k,i}\right) - \frac{1}{2}\left(u^*_{i,k} + u^*_{k,i}\right)\right\} \mathrm{d}V$$
$$= \frac{1}{V}\int_A \left\{\frac{1}{2}\left(u_i n_k + u_k n_i\right) - \frac{1}{2}\left(u^*_i n_k + u^*_k n_i\right)\right\} \mathrm{d}A. \quad (2)$$

For a cubic RVE like the Kelvin cell, the local displacements at the boundary are in the Cartesian coordinate system

$$u_i^{j+} = \bar{\varepsilon}_{ik} {x_k}^{j+} + u_i^{*j+}, \quad (3)$$
$$u_i^{j-} = \bar{\varepsilon}_{ik} {x_k}^{j-} + u_i^{*j-}, \quad (4)$$

where the upper index "$j+$" means the positive and "$j-$" the negative orientated boundary in *j*-direction. The chosen boundary conditions ensure periodicity. Additionally, the Kelvin cell and the applied loads are point symmetric regarding the center of the RVE. This ensures that we have equal displacement fluctuations and tractions with opposite signs at opposite boundaries.

$${u_i}^{*j+} = {u_i}^{*j-}, \quad (5)$$
$${t_i}^{j+} = -{t_i}^{j-}. \quad (6)$$

This makes sure that the displacement fluctuation term $\frac{1}{2}(u^*_i n_k + u^*_k n_i)$ in Eq. (2) vanishes. The average stresses on the macro-scale also called as global stresses and strains for the RVE are (Hill, 1972)

$$\bar{\sigma}_{ik} = \frac{1}{V}\int_V \sigma_{ik}\, \mathrm{d}V = \frac{1}{V}\int_A t_i\, x_k \mathrm{d}A, \quad (7)$$

$$\bar{\varepsilon}_{ik} = \frac{1}{V}\int_A \frac{1}{2}\left(u_i n_k + u_k n_i\right) \mathrm{d}A. \quad (8)$$

Thus the Hill-Mandel condition is fulfilled. The difference of Eq. (3) and Eq. (4) can be written as

$${u_i}^{j+} - {u_i}^{j-} = \bar{\varepsilon}_{ik}\left({x_k}^{j+} - {x_k}^{j-}\right) = \bar{\varepsilon}_{ik} \Delta x_k^j, \quad (9)$$

where Δx_k^j is the dimension of the RVE. The effective elastic properties of the Kelvin cell are described by Hooke's law

$$\bar{\sigma}_{ij} = \bar{C}_{ijkl}\bar{\varepsilon}_{kl}, \quad (10)$$

with the effective elasticity tensor $\bar{C}_{ijkl}$. Written in Voigt's notation, we have

$$\bar{\sigma}_\alpha = [\,\bar{\sigma}_{11}, \bar{\sigma}_{22}, \bar{\sigma}_{33}, \bar{\sigma}_{12}, \bar{\sigma}_{13}, \bar{\sigma}_{23}]^T \equiv [\,\bar{\sigma}_1, \bar{\sigma}_2, \bar{\sigma}_3, \bar{\sigma}_4, \bar{\sigma}_5, \bar{\sigma}_6]^T, \quad (11)$$
$$\bar{\varepsilon}_\beta = [\,\bar{\varepsilon}_{11}, \bar{\varepsilon}_{22}, \bar{\varepsilon}_{33}, 2\bar{\varepsilon}_{12}, 2\bar{\varepsilon}_{13}, 2\bar{\varepsilon}_{23}]^T \equiv [\,\bar{\varepsilon}_1, \bar{\varepsilon}_2, \bar{\varepsilon}_3, \bar{\varepsilon}_4, \bar{\varepsilon}_5, \bar{\varepsilon}_6]^T. \quad (12)$$

For a complete anisotropic case Eq. (10) simplifies to

$$\bar{\sigma}_\alpha = \bar{C}_{\alpha\beta}\bar{\varepsilon}_\beta \ . \quad (13)$$

Due to the symmetry $\bar{C}_{\alpha\beta} = \bar{C}_{\beta\alpha}$, the stiffness tensor has 21 independent elastic constants for the general anisotropic linear elastic solid. The Kelvin cell has a cubic symmetry and therefore only contains 3 independent elastic constants. For a coordinate system with basis vectors pointing into the crystallographic axes <100>, <010>, <001> the elastic constants are

$$\bar{C}_{11} = \bar{C}_{22} = \bar{C}_{33},\ \bar{C}_{12} = \bar{C}_{13} = \bar{C}_{23},\ \bar{C}_{44} = \bar{C}_{55} = \bar{C}_{66}. \quad (14)$$

$$\bar{C}_{11} = \frac{(1-\bar{\nu})\bar{E}}{(1+\bar{\nu})(1-2\bar{\nu})},\ \bar{C}_{12} = \frac{\bar{\nu}\bar{E}}{(1+\bar{\nu})(1-2\bar{\nu})},\ \bar{C}_{66} = \bar{G}. \quad (15)$$

Inversely, if the elastic constants are known we can define the elastic properties also by the engineering elastic modulus $\bar{E} = \frac{(\bar{C}_{11}-\bar{C}_{12})(\bar{C}_{11}+2\bar{C}_{12})}{(\bar{C}_{11}+\bar{C}_{12})}$, the Poisson's ratio $\bar{\nu} = \frac{\bar{C}_{12}}{(\bar{C}_{11}+\bar{C}_{12})}$ and the shear modulus $\bar{G} = \bar{C}_{66}$. The anisotropy ratio is defined as $A_f = \frac{2\bar{C}_{66}}{(\bar{C}_{11}-\bar{C}_{12})}$.

2.3 Implementation in ABAQUS

2.3.1 Geometric model

The RVE of a Kelvin cell foam is shown in Fig. 1. All struts are cylinders with a length l=1. Thus the structure length of the RVE is L=2$\sqrt{2}l$. The simple theoretical relation between relative density and strut radius is $\rho = \frac{3\pi r^2}{2\sqrt{2}l^2}$ (Zhu, 1997), which neglects the overlap of struts at the node. By analyzing the geometry of FEM volume models, we found that the relation between strut radius r and relative density ρ is $r = \left(\frac{\rho}{a}\right)^{\frac{1}{b}}$. In this simulation we found the parameters as a=2.4289 and b=1.9023. We focus on 1% and 2% relative density, which results in the strut radii of r=0.0557l and r=0.0802l, respectively. In order to simplify the simulation and to study only the structural influence on the mechanical properties, the Young's modulus E=1MPa and Poisson's ratio ν=0.25 are chosen as elastic material constants for the struts within the FEM model.

2.3.2 Boundary conditions

Because of the geometric symmetry of the Kelvin cell, boundary surfaces are parallel and have the same shape at opposite sides. The periodic boundary conditions for the displacements are applied by using "equation" constraints which need a periodic surface mesh on each axis. But the tetrahedral meshes generated by the ABAQUS software do not guarantee that every single point on the boundary surface may have a corresponding point on the opposite surface. So we copy one master surface mesh to the positive RVE surface as mirror surface and use "tie" constraints to

connect the mirror surface and the original surface to make these two surfaces deform simultaneously as shown in Fig. 2 (Storm et al., 2013). We set three reference points as master nodes on each direction respectively. Then the equation constraints between the corresponding points on the master surface and the mirror surface respectively and the reference points are built

$$u_i{}^{j+} - u_i{}^{j-} = \bar{\varepsilon}_{ik}\left(x_k{}^{j+} - x_k{}^{j-}\right) = \bar{\varepsilon}_{ik}\Delta x_k^j = u_i{}^{\mathrm{ref}_j}, \tag{16}$$

where $u_i{}^{\mathrm{ref}_j}$ are the given displacements u_i at reference points j.

For any cube-like RVE model $\Delta x_k^j = L$ is constant. Then the strains can be calculated as

$$\bar{\varepsilon}_{ik} = \frac{u_i{}^{\mathrm{ref}_j}}{\Delta x_k^j}. \tag{17}$$

In addition, the antiperiodic reciprocal surface tractions must be fulfilled. Due to the point symmetry of the Kelvin cell this is satisfied automatically.

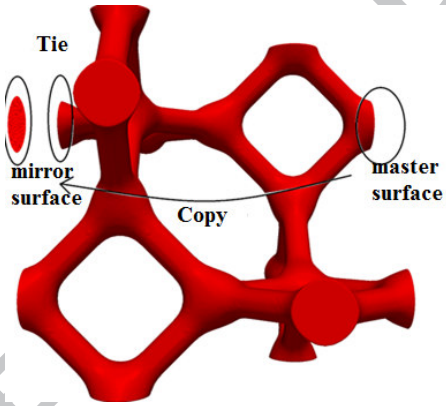

Fig. 2 Modelling periodic boundary conditions on models without periodic surface meshes (Storm et al., 2013).

2.3.3 Computation of the stiffness tensor

Since the analysis is done within the elastic and small deformation region, the superposition principle can be applied. One simple load case is enough to determine the components of the stiffness matrix for a Kelvin cell. In this load case a uniaxial deformation and a shear deformation within the corresponding orthogonal plane $\bar{\varepsilon} = (\bar{\varepsilon}_1, 0, 0, 0, 0, \bar{\varepsilon}_6)$ are applied simultaneously. From the FEM calculation we get the reaction forces at the reference points and divide them by the nominal area of the cross section in each direction, which results in components of the average stress tensor for the RVE.

$$\bar{\sigma}_1 = \bar{C}_{11}\bar{\varepsilon}_1 = \frac{F_1{}^{\mathrm{ref}_1}}{A_{\mathrm{nom}}},\ \bar{\sigma}_2 = \bar{C}_{12}\bar{\varepsilon}_1 = \frac{F_2{}^{\mathrm{ref}_1}}{A_{\mathrm{nom}}}, \tag{18}$$

$$\bar{C}_{11} = \bar{\sigma}_1/\bar{\varepsilon}_1,\ \bar{C}_{12} = \bar{\sigma}_2/\bar{\varepsilon}_1, \tag{19}$$

$$\bar{\tau}_{23} = \bar{\sigma}_6 = \bar{C}_{66}\bar{\varepsilon}_6 = \frac{1}{2}\left(\frac{{F_3}^{\mathrm{ref}_2}}{A_{\mathrm{nom}}} + \frac{{F_2}^{\mathrm{ref}_3}}{A_{\mathrm{nom}}}\right). \tag{20}$$

In the above equations ${F_i}^{\mathrm{ref}_j}$ denotes the reaction force F into x_i direction at the respective reference point j, A_{nom} the nominal area of each surface of the RVE which is L^2.

2.3.4 Failure limit surface

A failure limit surface is defined by a set of points in the homogenized stress space, where a local failure criterion on the micro-scale reaches a critical value. Typically, the stress space is spanned by the three homogenized principal stresses $(\bar{\sigma}_1, \bar{\sigma}_2, \bar{\sigma}_3)$ (not in Voigt's notation). For convenience the failure limit surface can be expressed using a cylindrical coordinate system ($\bar{\sigma}_{\mathrm{r}}$, θ, $\bar{\sigma}_{\mathrm{z}}$), which is calculated from the principal stresses by

$$\bar{\sigma}_{\mathrm{r}} = \sqrt{2J_2},\quad \cos 3\theta = \frac{J_3}{2}\left(\frac{3}{J_2}\right)^{3/2},\quad \bar{\sigma}_{\mathrm{z}} = \frac{I_1}{\sqrt{3}}. \tag{21}$$

Here $\bar{\sigma}_{\mathrm{z}}$ denotes a stress coordinate along the hydrostatic axis in principal stress space, $\bar{\sigma}_{\mathrm{r}}$ denotes a stress coordinate along the deviatoric axis in principal stress space, $\bar{\sigma}_{\mathrm{I}}$, $\bar{\sigma}_{\mathrm{II}}$, $\bar{\sigma}_{\mathrm{III}}$ are projections of $\bar{\sigma}_1$, $\bar{\sigma}_2$, $\bar{\sigma}_3$ on the π-plane, θ denotes the angular coordinate as depicted in Fig. 3, which is also known as positive cosine Lode angle. It starts from $\bar{\sigma}_{\mathrm{I}}$ and has the range [0, π/3]. The principal stresses and the cylindrical stress coordinates are related by

$$\begin{bmatrix}\bar{\sigma}_1\\ \bar{\sigma}_2\\ \bar{\sigma}_3\end{bmatrix} = \frac{1}{\sqrt{3}}\begin{bmatrix}\bar{\sigma}_{\mathrm{z}}\\ \bar{\sigma}_{\mathrm{z}}\\ \bar{\sigma}_{\mathrm{z}}\end{bmatrix} + \sqrt{\frac{2}{3}}\bar{\sigma}_{\mathrm{r}}\begin{bmatrix}\cos\theta\\ \cos(\theta - \frac{2\pi}{3})\\ \cos(\theta + \frac{2\pi}{3})\end{bmatrix}. \tag{22}$$

In the equations above we make use of three stress invariants: $\bar{I}_1 = \bar{\sigma}_{ii} = \bar{\sigma}_1 + \bar{\sigma}_2 + \bar{\sigma}_3$, $\bar{J}_2 = \frac{1}{2}\bar{\sigma}_{ij}^D\bar{\sigma}_{ij}^D = \frac{1}{6}[(\bar{\sigma}_1 - \bar{\sigma}_2)^2 + (\bar{\sigma}_2 - \bar{\sigma}_3)^2 + (\bar{\sigma}_3 - \bar{\sigma}_1)^2]$, $\bar{J}_3 = \bar{\sigma}_{ik}^D\bar{\sigma}_{kj}^D\bar{\sigma}_{ij}^D$, where $\bar{\sigma}_{ij}^D = \bar{\sigma}_{ij} - \frac{\bar{I}_1}{3}\delta_{ij}$ is the deviatoric stress tensor.

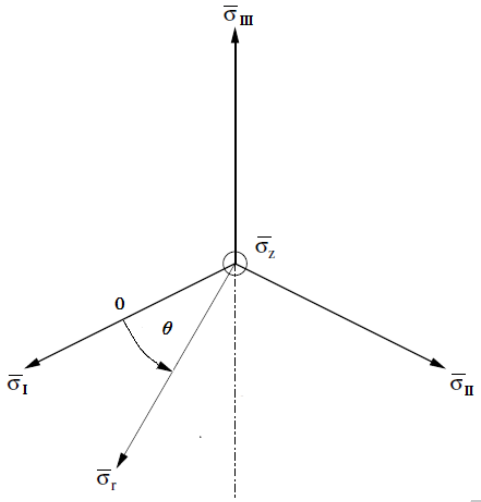

Fig. 3 Cylindrical coordinate system, θ starts from $\bar{\sigma}_1$.

A brittle material like ceramic foam is more sensitive to tension than to compression. The failure behavior under global multi-axial tension loading condition is discussed. To compute a failure limit surface for a periodic structure the following steps are necessary:

- Compute the elastic constants $\bar{C}_{ij}$ as described in section 2.3.3
- Define a set of stress states in cylindrical coordinates ($\bar{\sigma}_r$, θ, $\bar{\sigma}_z$) as shown in Fig. 4a, which comprises one-fourth of an ellipse on the $\bar{\sigma}_z - \bar{\sigma}_r$ plane divided into 9 equal angular segments. The intercept in $\bar{\sigma}_r$ axis is $\sqrt{\kappa}/\kappa$ and in $\bar{\sigma}_z$ axis is $\sqrt{\kappa}$ where κ denotes an elongation factor of the ellipsoid, here we set $\kappa = 10$. The range of angle θ is $\theta = \left[0, \frac{\pi}{3}\right] = [0, 60°]$ and divided into 8 equal segments. Translating the stress states to the principal stresses coordinate system ($\bar{\sigma}_1, \bar{\sigma}_2, \bar{\sigma}_3$) by using Eq. (22), it forms the red segment of points in Fig. 4b. The other segments in Fig. 4b can be constructed by cyclic permutations of $\bar{\sigma}_1$, $\bar{\sigma}_2$ and $\bar{\sigma}_3$. Finally, there are totally 90 points (each point stands for a load case) in cylindrical coordinates ($\bar{\sigma}_r$, θ, $\bar{\sigma}_z$) in Fig. 4a.
- Compute the corresponding strains $\bar{\varepsilon}_i = \bar{C}_{ij}^{-1}\bar{\sigma}_j$ and apply them as displacement boundary conditions for the unit cell according to Eq. (17).
- Apply FEM to solve the boundary value problem for the Kelvin cell.

- Determine for each loading case the local maximum stress σ_{locf} according to the chosen failure criterion. σ_{c} is the critical material strength assumed as unit value 1 MPa. When $\sigma_{\mathrm{locf}} = \sigma_{\mathrm{c}}$, the material is assumed to fail.
- Scale the global principal stresses $(\bar{\sigma}_1, \bar{\sigma}_2, \bar{\sigma}_3)$ by a factor $\lambda = \sigma_{\mathrm{c}}/\sigma_{\mathrm{locf}}$ to get the stress state $(\bar{\sigma}_1\lambda,\ \bar{\sigma}_2\lambda,\ \bar{\sigma}_3\lambda)$ which describes one point on an iso-surface of failure. In order to allow a linear scaling, the failure criterion has to be homogeneous of degree one in the stress tensor and the local stress must be linearly dependent on global stresses $\bar{\sigma}_1$, $\bar{\sigma}_2$ and $\bar{\sigma}_3$.

To analyze the anisotropic properties, three kinds of global loading are applied with respect to the coordinate axes of the RVE. Loading case S<100> only contains principal stresses, and the principal stress axes are consistent with the axes of RVE. Then rotate the stress state along the second principal stress axis by 45° to get loading case S<101>, and then rotate the stress state along the new third principal axis to get loading case S<111> to make sure that the first principal stress axis of S<111> is consistent with the space diagonal of the RVE.

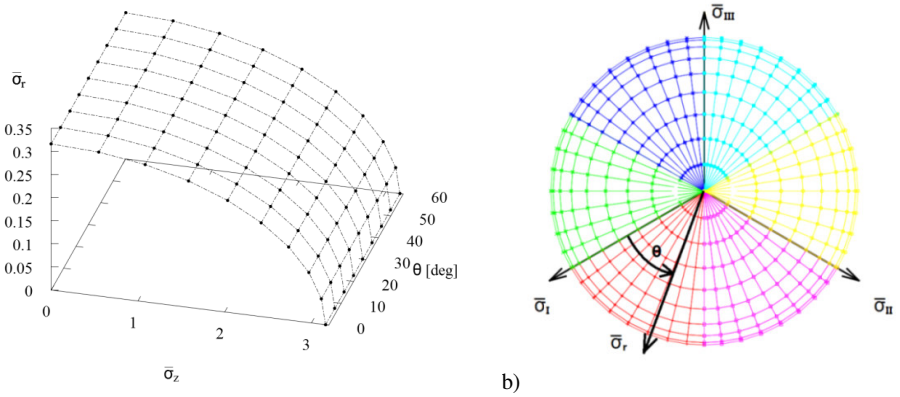

a) b)

Fig. 4 a) Initial stress states in the cylindrical coordinate system. Each point stands for a loading case. b) Initial stress states in principal stress space (projected to the π-plane).

2.3.5 Weibull stress

The probability function for the brittle fracture strength of a solid subject to a homogeneous stress field can be expressed by the Weibull distribution. In case of complex stress state like in foams, Weibull statistic was extended by the weakest link statistics. It has been widely used to estimate the probability that a given sample will fail under a given load.

$$P(\sigma_{\mathrm{w}}) = 1 - \exp\left\{-\left(\frac{\sigma_{\mathrm{w}}}{\sigma_{\mathrm{u}}}\right)^{m}\right\}, \tag{23}$$

where m and σ_u denote the Weibull modulus (also named as shape parameter) and the scale parameter of the Weibull distribution, respectively. In particular, m defines the shape of the probability density function and quantifies the statistical scatter. In this work, we assumed m=6.3, which is a typical value for ceramic.

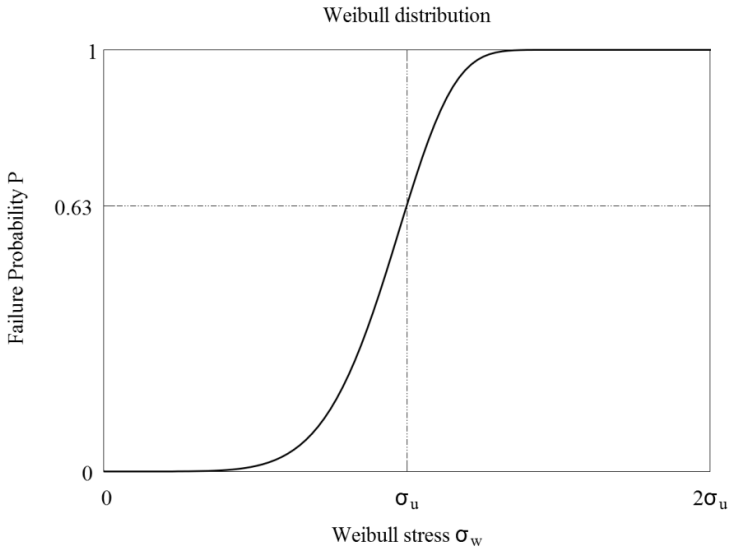

Fig. 5 Weibull failure probability distribution.

The Weibull stress σ_w is defined (Beremin, 1983) as

$$\sigma_w = \left[\frac{1}{V_0}\int_{V_0} \sigma_1^m dV\right]^{1/m}, \tag{24}$$

or in a FEM convenient form

$$\sigma_w = \left[\sum_{i=1}^{n_e} (\sigma_1^i)^m \frac{V_i}{V_0}\right]^{1/m}, \tag{25}$$

where V_0 is a reference volume, V_i is the volume of the i-th element integration point experiencing the maximum principal stress σ_1^i, n_e is the number of element integration points within the model. The principle of independent action (PIA) (Barnett et al., 1967; Freudenthal, 1968; Manderscheid, 1987) considers the influence of all principal stresses on the Weibull stress. In this paper a modified PIA stress was used and σ_1^i in Eq. (25) is replaced by an equivalent stress

$$\sigma_{eq}^i = \left[\left(\frac{\sigma_1+|\sigma_1|}{2}\right)^m + \left(\frac{\sigma_2+|\sigma_2|}{2}\right)^m + \left(\frac{\sigma_3+|\sigma_3|}{2}\right)^m\right]^{1/m}, \tag{26}$$

and the Weibull stress is expressed as

$$\sigma_w = \left[\sum_{i=1}^{n_e} (\sigma_{eq}^i)^m \frac{V_i}{V_0}\right]^{1/m}. \tag{27}$$

This criterion postulates that the Weibull stress σ_w of the RVE controls the fracture probability.

2.3.6 The Bigoni - Piccolroaz failure criterion

The numerically computed failure limit surfaces might be described in an analytical form. Bigoni and Piccolroaz (Bigoni, 2012; Bigoni and Piccolroaz, 2004) proposed the following structure for a universal failure criterion.

$$F(\bar{\sigma}) = f(\bar{\sigma}_z) + \frac{\bar{\sigma}_r}{g(\theta)} = 0. \tag{28}$$

Here the function $f(\bar{\sigma}_z)$ describes the dependence on the hydrostatic stress and $g(\theta)$ the dependence on the Lode angle. Eq. (28) can be written as a function for $\bar{\sigma}_r$:

$$\bar{\sigma}_r = -f(\bar{\sigma}_z)g(\theta). \tag{29}$$

In this paper we assume the failure function as follows

$$f(\bar{\sigma}_z) = -B\left(\frac{A-\bar{\sigma}_z}{A}\right)^n, \tag{30}$$

$$g(\theta) = \frac{1}{\cos\left\{[1+C]\frac{\pi}{6} - \frac{1}{3}\cos^{-1}[D\cos(3\theta)]\right\}}, \tag{31}$$

and we get

$$\bar{\sigma}_r = \frac{B\left(\frac{A-\bar{\sigma}_z}{A}\right)^n}{\cos\left\{[1+C]\frac{\pi}{6} - \frac{1}{3}\cos^{-1}[D\cos(3\theta)]\right\}}. \tag{32}$$

The parameters *A* and *B* describe the size of the failure limit surface in hydrostatic and deviatoric stress direction. The parameters *n*, *C* and *D* influence the shape of the failure limit surface.

3. Results

3.1 Elastic constants

In this paper, beam models as well as volume models are used in FEM-analysis of Kelvin cell. As explained in Section 2.3.1, the exact strut radius differs somewhat from Zhu's model. The beam model ignores the material overlapped at nodes and the stress concentration at the corners. The volume model is more realistic than the beam model. Comparing with Zhu's (Zhu, 1997) result volume models are stiffer than beam models. Poisson's ratios of different models are almost the same nearly 0.5. In Table 1 the differences between volume model, beam model and Zhu's beam model are listed. The differences between beam and volume models increase with increasing relative density.

Table 1 Comparison of elastic constants for different models (Err1=(Vol-Beam)/Beam, Err2=(Vol-Zhu)/Zhu, Err3=(Beam-Zhu's)/Zhu's)

	Volume model	Beam model	Err1(%)	Zhu's result	Err2(%)	Err3(%)
$\bar{E}$ (1%) [Mpa]	7.17E-05	6.21E-05	13.3	5.95E-05	20.5	4.52
$\bar{E}$ (2%) [Mpa]	3.19E-04	2.58E-04	19.3	2.36E-04	35.4	9.28
$\bar{G}$ (1%) [Mpa]	2.20E-05	2.07E-05	5.98	1.95E-05	12.9	6.14
$\bar{G}$ (2%) [Mpa]	9.54E-05	8.69E-05	9.78	7.76E-05	23.0	12.0
$\bar{v}$ (1%)	4.90E-01	4.91E-01	-0.18	4.91E-01	-0.19	-0.02
$\bar{v}$ (2%)	4.79E-01	4.82 E-01	-0.56	4.82E-01	-0.63	-0.07

3.2 Maximum principal stress criterion – FEM volume model

One common failure criterion for brittle materials is the maximum principal stress criterion. Let us order the local stresses as $\sigma_1 > \sigma_2 > \sigma_3$. The criterion assumes that a material fails when one of the principal stresses σ_i exceeds the uniaxial tensile or compressive strength of the material σ_c. If we suppose that tension and compression strength of the strut material are the same, then the maximum local stress is $\sigma_{\mathrm{locf}} = \sigma_{\max} = \max(|\sigma_1|, |\sigma_3|)$. The scale factor $\lambda = \frac{\sigma_c}{\sigma_{\mathrm{locf}}} = \frac{1}{\sigma_{\max}}$ is used to draw a failure limit surface, which describes a global loading limit, where locally the material reaches the strength limit. The corresponding failure limit surfaces are shown in Figs. 6-9 for relative densities of 1% (left) and 2% (right). The characteristic Lode angles are 0°, 15°, 30°, 60°. It is clearly to see that the failure limit surface is strongly dependent on the global loading direction.

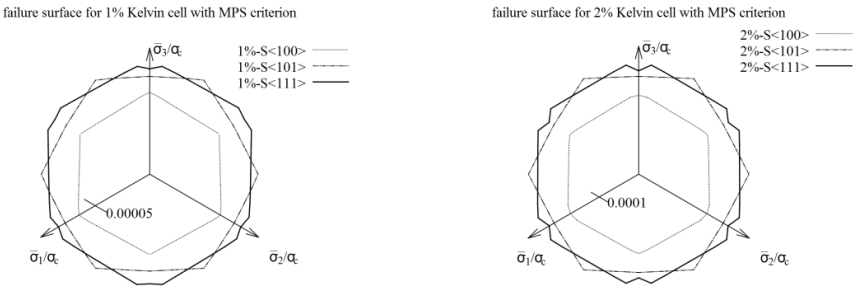

Fig. 6 Failure limit surface on the π-plane using maximum principal stress criterion (tic marks represent the absolute values).

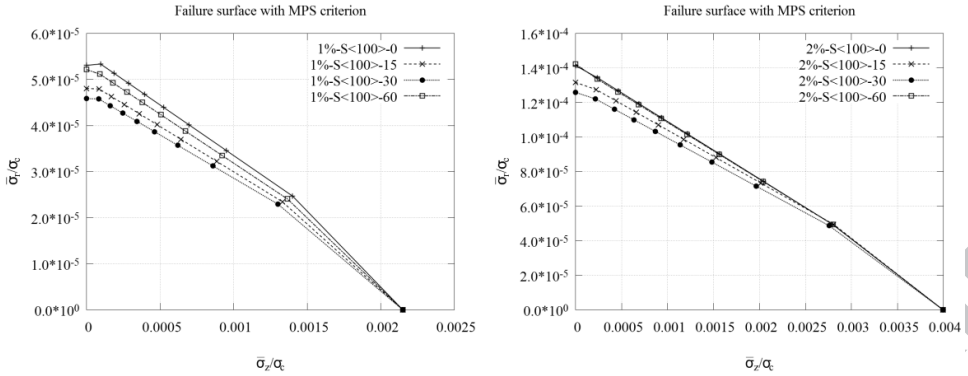

Fig. 7 The influence of Lode angle on meridional profile under global loading case S<100> using maximum principal stress criterion.

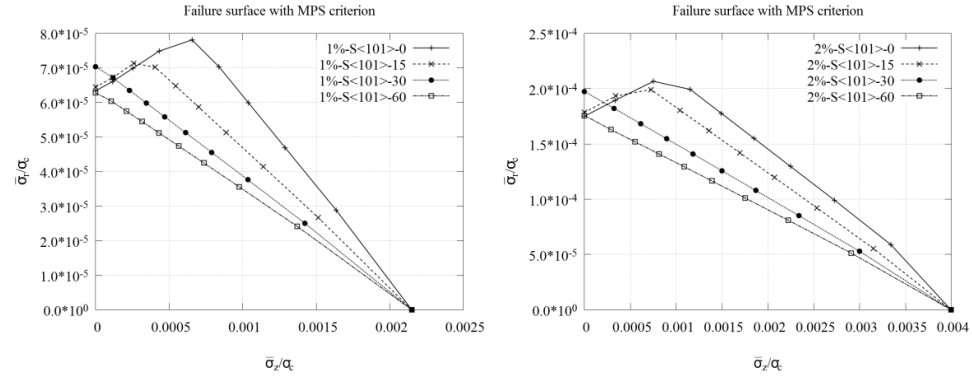

Fig. 8 The influence of Lode angle on meridional profile under global loading case S<101> using maximum principal stress criterion.

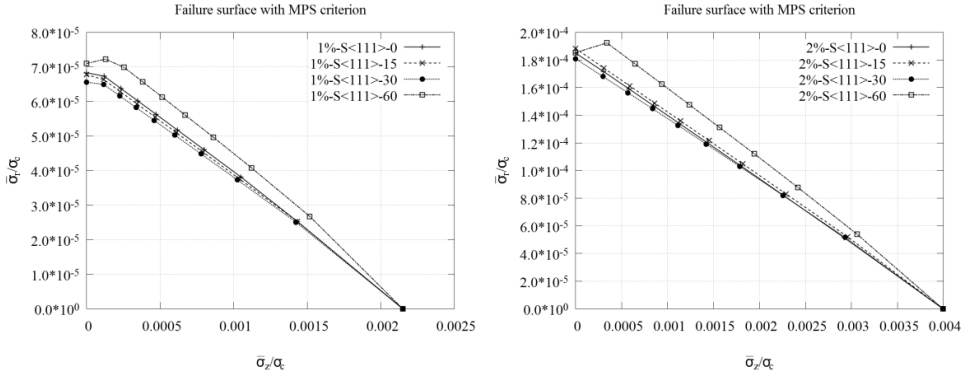

Fig. 9 The influence of Lode angle on meridional profile under global loading case S<111> using maximum principal stress criterion.

3.3 Weibull stress criterion - FEM volume model

For the computation of the Weibull stress, the concept of independent action (PIA) is applied according to Eq. (26) and Eq. (27). Assuming the Weibull stress criterion, the structure is more sensitive to global tension than to global compression, so we focus on the tension part. The normalized failure limit surfaces have parabolic shape on the $\bar{\sigma}_z - \bar{\sigma}_r$ plane. The failure limit surfaces for 1% and 2% relative density have a similar shape but are different in size as depicted in Figs. 10-13. Fig. 10 shows projections of failure limit surface on the deviatoric plane. Figs.11-13 show failure limit surfaces as meridional profiles in the cylindrical coordinate system. The failure limit surface corresponding to the Weibull stress criterion also shows pronounced anisotropic properties. Under global loading S<100> the Lode angle θ has only a small influence on $\bar{\sigma}_r$. Under global loading <101> $\bar{\sigma}_r$ decreases with increasing angle θ, whereas under global loading <111> $\bar{\sigma}_r$ increases with increasing angle θ.

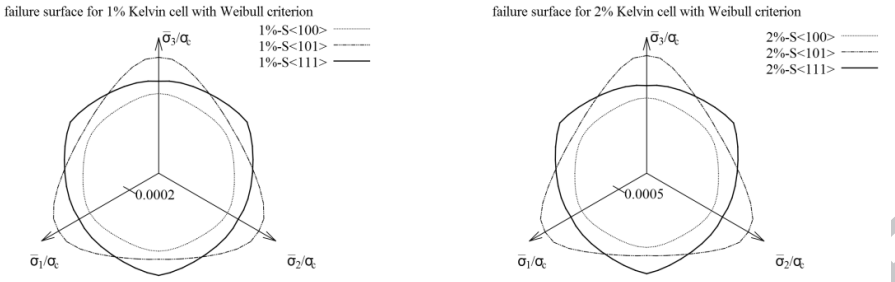

Fig. 10 Failure limit surface for a Kelvin cell on the π-plane using Weibull stress criterion (tic marks represent the absolute values).

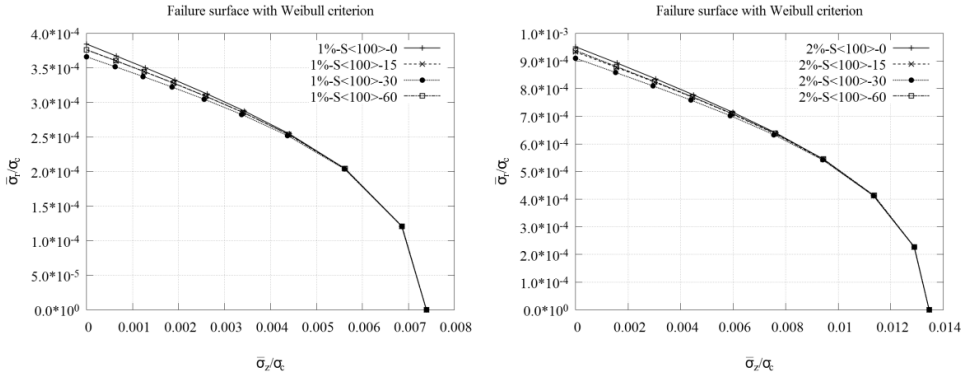

Fig. 11 The influence of Lode angle on meridional profile under global loading case S<100> using Weibull stress criterion.

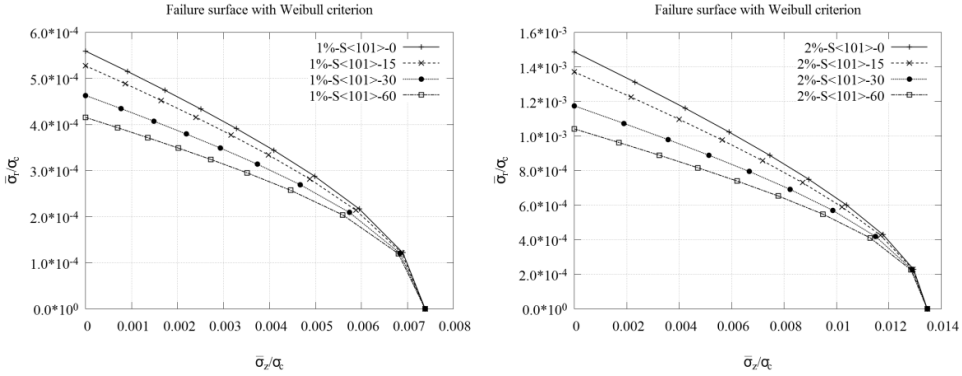

Fig. 12 The influence of Lode angle on meridional profile under global loading S<101> using Weibull stress criterion.

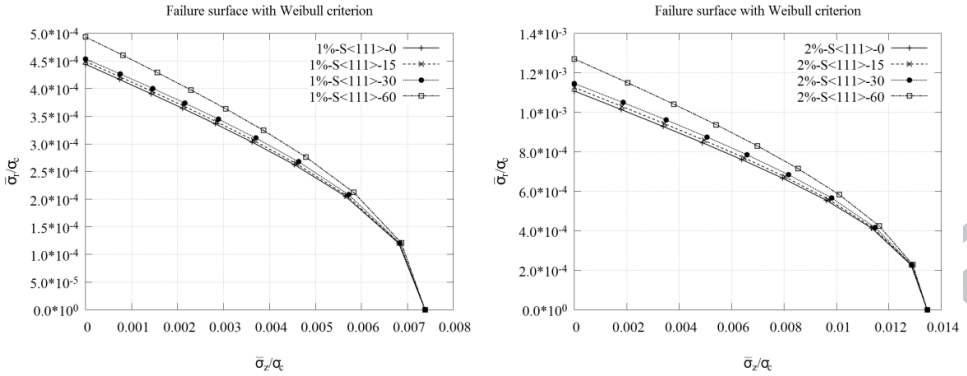

Fig. 13 The influence of Lode angle on meridional profile under global loading S<111> using Weibull stress criterion.

3.4 Weibull stress criterion - Beam Models

Under the same conditions the failure limit surfaces have been calculated by using a beam model. Each strut is modelled using 8 Timoshenko beam elements having a circular cross section. The shape of failure limit surfaces is similar with those of the volume model, but the global loading case has only a small influence on the failure limit surface shape. The failure limit surfaces of the beam models projected onto the π-plane are shown in Fig. 14. They have a similar shape for different relative densities but are different from the corresponding volume models.

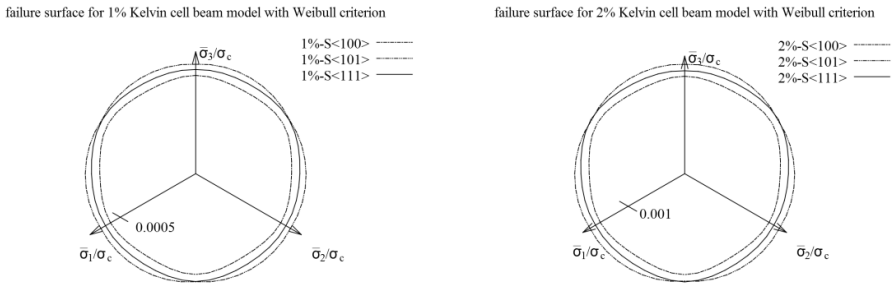

Fig. 14 Failure limit surface on the π-plane for beam model using Weibull stress criterion (tic marks represent the absolute values).

The comparison of effective normalized failure stresses according to both local maximum principal stress failure criterion and effective Weibull stress criterion are listed in Table 2 and 3. Volume models show a significantly smaller effective failure stress than beam models, because beam models neglect the stress concentrations at the foam nodes, where four struts met.

Table 2 Effective normalized failure stress according to the local maximum principal stress failure criterion

				S<100>			S<101>			S<111>		
$\bar{\sigma}_r$	θ	$\bar{\sigma}_z$	ρ	Volume	Beam	Err(%)	Volume	Beam	Err(%)	Volume	Beam	Err(%)
-	0	0	1%	5.31E-05	1.72E-04	-69.2	6.34E-05	1.76E-04	-64.0	6.83E-05	1.66E-04	-58.9
-	0	0	2%	1.41E-04	5.12E-04	-72.4	1.75E-04	5.25E-04	-66.7	1.85E-04	4.92E-04	-62.4
-	15	0	1%	4.80E-05	1.55E-04	-69.1	6.44E-05	1.77E-04	-63.7	6.78E-05	1.52E-04	-55.4
-	15	0	2%	1.32E-04	4.63E-04	-71.6	1.77E-04	5.29E-04	-66.2	1.88E-04	4.53E-04	-58.5
-	30	0	1%	4.58E-05	1.51E-04	-69.6	6.68E-05	1.78E-04	-62.5	6.56E-05	1.47E-04	-55.5
-	30	0	2%	1.26E-04	4.50E-04	-72.0	1.97E-04	5.32E-04	-62.9	1.81E-04	4.40E-04	-58.9
-	60	0	1%	5.21E-05	1.72E-04	-69.7	6.28E-05	1.76E-04	-64.4	7.10E-05	1.66E-04	-57.3
-	60	0	2%	1.42E-04	5.12E-04	-72.2	1.76E-04	5.25E-04	-66.5	1.85E-04	4.92E-04	-62.3
0	-	-	1%	2.15E-03	5.97E-03	-64.0	2.15E-03	5.97E-03	-64.0	2.15E-03	5.97E-03	-64.0
0	-	-	2%	3.99E-03	1.24E-02	-67.7	3.99E-03	1.24E-02	-67.7	3.99E-03	1.24E-02	-67.7

Table 3 Effective normalized failure stress according to Weibull stress failure criterion

				S<100>			S<101>			S<111>		
$\bar{\sigma}_r$	θ	$\bar{\sigma}_z$	ρ	Volume	Beam	Err(%)	Volume	Beam	Err(%)	Volume	Beam	Err(%)
-	0	0	1%	3.84E-04	4.61E-04	-16.6	5.59E-04	5.13E-04	8.95	4.44E-04	4.88E-04	-9.07
-	0	0	2%	9.51E-04	1.22E-03	-22.0	1.49E-03	1.37E-03	8.65	1.11E-03	1.29E-03	-14.0
-	15	0	1%	3.76E-04	4.54E-04	-17.2	5.27E-04	5.18E-04	1.90	4.49E-04	4.88E-04	-8.06
-	15	0	2%	9.33E-04	1.20E-03	-22.5	1.37E-03	1.38E-03	-0.48	1.13E-03	1.29E-03	-12.9
-	30	0	1%	3.66E-04	4.49E-04	-18.6	4.63E-04	5.18E-04	-10.5	4.54E-04	4.89E-04	-7.12
-	30	0	2%	9.10E-04	1.19E-03	-23.9	1.17E-03	1.38E-03	-14.6	1.15E-03	1.30E-03	-11.7
-	60	0	1%	3.76E-04	4.73E-04	-20.4	4.15E-04	5.07E-04	-18.1	4.93E-04	5.06E-04	-2.44
-	60	0	2%	9.38E-04	1.26E-03	-25.8	1.04E-03	1.34E-03	-22.6	1.27E-03	1.35E-03	-6.18
0	-	-	1%	7.38E-03	7.52E-03	-1.76	7.38E-03	7.52E-03	-1.76	7.38E-03	7.52E-03	-1.76
0	-	-	2%	1.35E-02	1.24E-02	8.76	1.35E-02	1.24E-02	8.76	1.35E-02	1.24E-02	8.76

3.5 The fit function for the Weibull model

The failure limit surfaces of both beam and volume model have similar shapes on the $\bar{\sigma}_z - \bar{\sigma}_r$ plane but different shapes on the π-plane. The failure limit surfaces can be approximated by the fit function. After scaling the global stresses $\bar{\sigma}_r$ and $\bar{\sigma}_z$ by the factor σ_w, Eq. (32) changes to:

$$\frac{\bar{\sigma}_r}{\sigma_w} = \frac{B\left(\frac{A-\frac{\bar{\sigma}_z}{\sigma_w}}{A}\right)^n}{\cos\left\{[1+C]\frac{\pi}{6} - \frac{1}{3}\cos^{-1}[D\cos(3\theta)]\right\}}, \quad (33)$$

where $\theta = [0, \frac{\pi}{3}] = [0, 60°]$. The parameters *A* and *B* can be expressed as $A = \frac{\pi(\frac{r}{l})^2}{\alpha}$ and $= \frac{\pi(\frac{r}{l})^3}{\beta}$. There are 5 parameters α, β, *C*, *D* and *n* to be determined.

From the expressions of parameters *A* and *B* we noticed that *A* has a relationship with the cross section area which means it is determined by the tensile strut stiffness and *B* has a relationship to the static moment determining the bending stiffness of the strut. From the function Eq. (33) and Figs. 11-13 we know that *A* is related to the maximum value of hydrostatic stress $\frac{\bar{\sigma}_z}{\sigma_w}$ and *B* is influenced by both $\frac{\bar{\sigma}_z}{\sigma_w}$ and $\frac{\bar{\sigma}_r}{\sigma_w}$. The parameters *C* and *D* are used to describe the shape of the deviatoric section. *n* describes the shape on the $\bar{\sigma}_z - \bar{\sigma}_r$ plane.

The failure limit surface looks like a half of a paraboloid. Figs. 15-17 compare the simulated failure limit surface and the corresponding fitted function for 1% relative density for both the volume model (left) and beam model (right). The solid lines stand for the fitted function and the dots represent the corresponding FEM results. The values for the parameters in Eq. (33) for the different relative densities and models (volume, beam) are given in Tables 4-6.

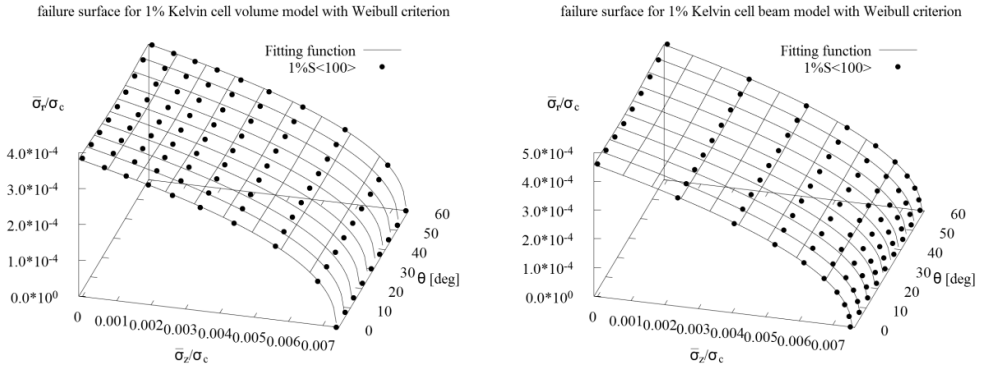

Fig. 15 The comparison between the failure function and 3D-FEM results with 1% relative density under loading case S<100> in the cylindrical coordinate system (left is volume model, right is beam model).

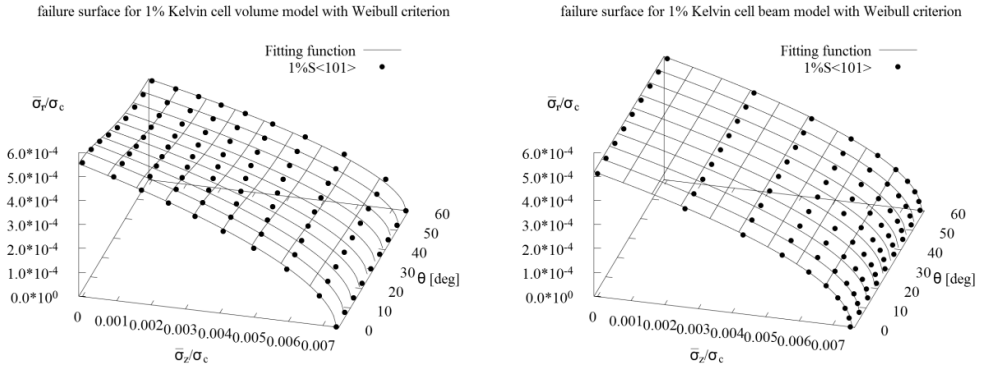

Fig. 16 The comparison between the failure function and 3D-FEM results with 1% relative density under loading case S<101> in the cylindrical coordinate system (left is volume model, right is beam model).

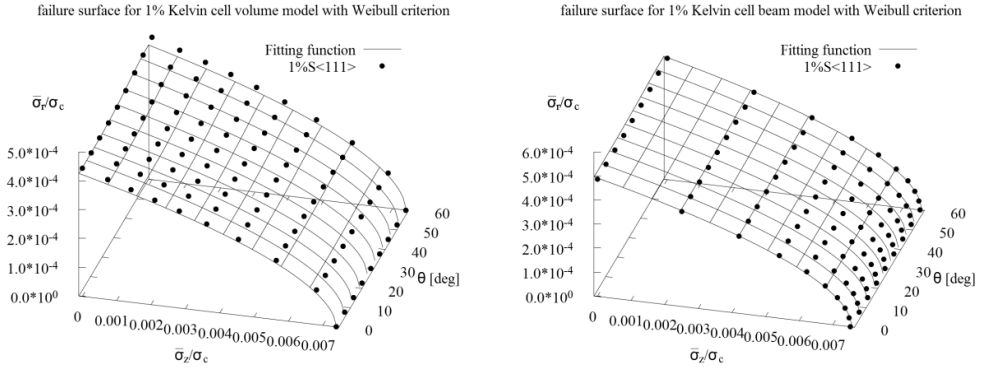

Fig. 17 The comparison between the failure function and 3D-FEM results with 1% relative density under loading case S<111> in the cylindrical coordinate system (left is volume model, right is beam model).

Table 4 The fitted parameters for both volume and beam models under global loading S<100>.

	1% volume	2% volume	1% beam	2% beam
α	1.31876	1.50161	1.28806	1.45582
β	1.47804	1.78745	1.20596	1.36759
C	0.04168	0.04517	-0.11779	-0.22710
D	0.62786	0.63586	0.58384	0.46270
n	0.42803	0.43919	0.48060	0.46382

Table 5 The fitted parameters for both volume and beam models under global loading S<101>.

	1% volume	2% volume	1% beam	2% beam
α	1.31876	1.50161	1.28806	1.45582
β	1.38287	1.62815	1.54042	1.78759
C	1.07277	1.07536	1.55485	1.60645
D	0.59551	0.67509	0.01295	0. 01728
n	0.54745	0.56079	0.51289	0.49984

Table 6 The fitted parameters for both volume and beam models under global loading S<111>.

	1% volume	2% volume	1% beam	2% beam
α	1.31876	1.50161	1.28806	1.45582
β	1.28540	1.47641	1.10143	1.26680
C	0.39350	-0.48071	-0.24363	-0.34227
D	-0.59905	0.62761	0.35806	0.36341
n	0.53367	0.53336	0.52302	0.48560

4 Conclusions

In this paper, at first the maximum principal stress criterion is used to prove that the failure limit surface of a Kelvin cell foam is anisotropic. Then, it is proposed that the probabilistic Weibull model can be used to describe the global failure limit surface of a foam structure, which is made from a brittle material like ceramic. The Weibull stress is a global equivalent stress for the heterogeneous local stress distribution. In this paper the calculation of Weibull stress is based on the principle of independent action and takes into consideration all three principal stresses. It is dependent on the global multi-axial stress state. The failure limit surface is calculated by scaling the

global stress state with the Weibull stress. The global stress states as well as the Weibull stress are determined using finite element simulations either using continuum or beam elements. With both techniques comparable results can be derived. The resulting failure limit surface describes an iso-surface where the failure probability is equal to 63%. For the Weibull stress criterion analytical functions have been found, consisting of parameters, which are determined by the cross section area and the static moment of the struts. In this way the results of present extensive numerical computations are made available for other researchers in a simple mathematical form. Analyses with beam models suggest that the global loading direction has only a small influence on the shape of failure limit surfaces. But simulations with volume models show that the failure limit surface is strongly depending on global loading. The reason is that beam models ignore the material overlap and the stress concentration at the foam nodes and. In conclusion, beam models can be used to describe the failure behavior of foam structure only under simple loading cases but under complex loading cases they neglect much important information. Therefore, volume models are more appropriate. The failure limit surfaces for the maximum principal stress criterion are more isotropic (hexagonal cross section shape) than the failure limit surfaces for the Weibull stress failure criterion, where we observe a compression-tension asymmetry which is depicted by the triangular cross section shape (especially for the S<101> loading case). Furthermore, the equivalent Weibull stress can be used to study the failure behavior of the RVE under different failure probabilities.

5 Acknowledgment

The authors gratefully acknowledge the financial support by the German Research Foundation (DFG) within the collaborative research center SFB 920 as well as the support from the EFRE fund of the European Union.

6 References

Aghdam, M., Smith, D., Pavier, M., 2000. Finite element micromechanical modelling of yield and collapse behaviour of metal matrix composites. Journal of the Mechanics and Physics of Solids 48, 499-528.

Altenbach, H., Bolchoun, A., Kolupaev, V.A., 2014. Phenomenological yield and failure criteria, Plasticity of Pressure-Sensitive Materials. Springer, pp. 49-152.

Amaral, P.M., Cruz Fernandes, J., Guerra Rosa, L., 2007. Weibull statistical analysis of granite bending strength. Rock Mechanics and Rock Engineering 41, 917-928.

Ashby, M.F., 2000. Metal foams: a design guide. Butterworth-Heinemann.

Barnett, R.L., Hermann, P.C., Wingfield, J.R., Connors, C.L., 1967. Fracture of brittle materials under transient mechanical and thermal loading. DTIC Document.

Beremin, F.M., 1983. A local criterion for cleavage fracture of a nuclear pressure vessel steel. Metallurgical Transactions A 14A, 2277-2287.

Bigoni, D., 2012. Nonlinear solid mechanics: bifurcation theory and material instability. Cambridge University Press.

Bigoni, D., Piccolroaz, A., 2004. Yield criteria for quasibrittle and frictional materials. International Journal of Solids and Structures 41, 2855-2878.

C Chen, T.L., NA Fleck, 1999. Effect of imperfections on the yielding of two-dimensional foams. Journal of the Mechanics and Physics of Solids 47, 2235-2272.

Danzer, R., Supancic, P., Pascual, J., Lube, T., 2007. Fracture statistics of ceramics – Weibull statistics and deviations from Weibull statistics. Engineering Fracture Mechanics 74, 2919-2932.

Dement'ev, A., Tarakanov, O., 1970. Effect of cellular structure on the mechanical properties of plastic foams. Polymer Mechanics 6, 519-525.

Demiray, S., Becker, W., Hohe, J., 2007. Numerical determination of initial and subsequent yield surfaces of open-celled model foams. International Journal of Solids and Structures 44, 2093-2108.

DeRuntz, J.A., Hoffman, O., 1969. The static strength of syntactic foams. Journal of Applied Mechanics 36, 551-557.

Deshpande, V., Fleck, N., 2000. Isotropic constitutive models for metallic foams. Journal of the Mechanics and Physics of Solids 48, 1253-1283.

Deshpande, V., Fleck, N., 2001. Multi-axial yield behaviour of polymer foams. Acta materialia 49, 1859-1866.

Freudenthal, A.M., 1968. Statistical approach to brittle fracture. Fracture 2, 591-619.

Fuis, V., Navrat, T., 2011. Calculation of the Ceramics Weibull Parameters. World Academy of Science, Engineering and Technology 58, 642-647.

Gao, X., Ruggieri, C., Dodds Jr, R.H., 1998. Calibration of Weibull stress parameters using fracture toughness data. International Journal of Fracture 92, 175-200.

Gibson, L., Ashby, M., Zhang, J., Triantafillou, T., 1989. Failure limit surfaces for cellular materials under multiaxial loads—I. Modelling. International Journal of Mechanical Sciences 31, 635-663.

Gibson, L.J., Ashby, M.F., 1999. Cellular solids: structure and properties. Cambridge University Press.

Gong, L., Kyriakides, S., 2005. Compressive response of open cell foams Part II: Initiation and evolution of crushing. International Journal of Solids and Structures 42, 1381-1399.

Gong, L., Kyriakides, S., Jang, W.Y., 2005a. Compressive response of open cell foams. Part I: Morphology and elastic properties. International Journal of Solids and Structures 42, 1355-1379.

Gong, L., Kyriakides, S., Triantafyllidis, N., 2005b. On the stability of Kelvin cell foams under compressive loads. Journal of the Mechanics and Physics of Solids 53, 771-794.

Hill, R., 1972. On constitutive macro-variables for heterogeneous solids at finite strain. Proceedings of the Royal Society of London. A. Mathematical and Physical Sciences 326, 131-147.

Jang, W.-Y., Kraynik, A.M., Kyriakides, S., 2008. On the microstructure of open-cell foams and its effect on elastic properties. International Journal of Solids and Structures 45, 1845-1875.

Jang, W.-Y., Kyriakides, S., 2009a. On the crushing of aluminum open-cell foams: Part I. Experiments. International Journal of Solids and Structures 46, 617-634.

Jang, W.-Y., Kyriakides, S., 2009b. On the crushing of aluminum open-cell foams: Part II analysis. International Journal of Solids and Structures 46, 635-650.

Jang, W.-Y., Kyriakides, S., Kraynik, A.M., 2010. On the compressive strength of open-cell metal foams with Kelvin and random cell structures. International Journal of Solids and Structures 47, 2872-2883.

Karolczuk, A., 2013. Modelling of stress gradient effect on fatigue life using Weibull based distribution function. Journal of Theoretical and Applied Mechanics 51, 297-311.

Klein, C.A., 2009. Characteristic strength, Weibull modulus, and failure probability of fused silica glass. Optical Engineering 48, 113401.

Laroussi, M., Sab, K., Alaoui, A., 2002. Foam mechanics: nonlinear response of an elastic 3D-periodic microstructure. International Journal of Solids and Structures 39, 3599-3623.

Lei Y, O'Dowd, N.P., Busso, E.P., 1998. weibull stress solutions for 2-d cracks in elastic and elastic-plastic materials. International Journal of Fracture 89, 245-268.

Manderscheid, J.M., 1987. Fracture Mechanics Concepts in Reliability Analysis of Monolithic Ceramics. Nondestructive Testing of High-Performance Ceramics, 59-72.

Mills, N.J., 2007. The high strain mechanical response of the wet Kelvin model for open-cell foams. International Journal of Solids and Structures 44, 51-65.

Minami, F., Brückner-Foit, A., Munz, D., Trolldenier, B., 1992. Estimation procedure for the Weibull parameters used in the local approach. International Journal of Fracture 54, 197-210.

O'Dowd, N.P., Lei, Y., Busso, E.P., 2000. Prediction of cleavage failure probabilities using the Weibull stress. Engineering Fracture Mechanics 67, 87-100.

Piccolroaz, A., Bigoni, D., 2009. Yield criteria for quasibrittle and frictional materials: A generalization to surfaces with corners. International Journal of Solids and Structures 46, 3587-3596.

Sridhar, I., Fleck, N., 2005. The multiaxial yield behaviour of an aluminium alloy foam. Journal of materials science 40, 4005-4008.

Storm, J., Abendroth, M., Zhang, D., Kuna, M., 2013. Geometry Dependent Effective Elastic Properties of Open-Cell Foams Based on Kelvin Cell Models. Advanced Engineering Materials 15, 1292-1298.

Sullivan, R.M., Ghosn, L.J., 2009. Shear moduli for non-isotropic, open cell foams using a general elongated Kelvin foam model. International Journal of Engineering Science 47, 990-1001.

Sullivan, R.M., Ghosn, L.J., Lerch, B.A., 2009. Application of an elongated Kelvin model to space shuttle foams. Journal of Spacecraft and Rockets 46, 411-418.

Takahashi, Y., Okumura, D., Ohno, N., 2010. Yield and buckling behavior of Kelvin open-cell foams subjected to uniaxial compression. International Journal of Mechanical Sciences 52, 377-385.

Thiyagasundaram, P., Sankar, B.V., K.Arakere, N., 2010. Multi-axial Failure Strengths of Open-Cell Foams with Tetrakaidecahedral Cells Using Finite Element Analysis, 51st AIAA/ASME/ASCE/AHS/ASC Structures, Structural Dynamics, and Materials Conference
18th, Orlando, Florida.

Warren, W., Kraynik, A., 1997. Linear elastic behavior of a low-density Kelvin foam with open cells. Journal of Applied Mechanics 64, 787-794.

Weibull, W., 1951. A Statistical Distribution Funtion of Wide Applicability. Journal of Applied Mechanics.

Yin, S., Bass, R., Williams, P., Ludwig, M., Keim, E., 2004. Application of a weibull stress model to predict the failure of surface and embedded cracks in large scale beams made of clad and unclad RPV steel, ASME/JSME 2004 Pressure Vessels and Piping Conference. American Society of Mechanical Engineers, pp. 69-76.

Zhu, H., Knott, J., Mills, N., 1997. Analysis of the elastic properties of opencell foams with tetrakaidecahedral cells. Journal of the Mechanics and Physics of Solids 45, 319-343.

Highlights

- We introduce Weibull failure surface under 63% failure probability
- We compare failure surface under Maximum principal stress criterion and Weibull stress criterion.
- We compare the volume model and beam model result to analysis the beam model limitation.
- We fitting the failure surface by Bigoni-Piccolroaz failure criterion